Front. Phys. 11(6), 114703 (2016)
DOI 10.1007/s11467-016-0603-4

RESEARCH ARTICLE

Viscosity, heat conductivity, and Prandtl number effects in the Rayleigh–Taylor Instability

Feng Chen[1,*], **Ai-Guo Xu**[2,3†], **Guang-Cai Zhang**[2]

[1] *School of Aeronautics, Shan Dong Jiaotong University, Jinan 250357, China*
[2] *National Key Laboratory of Computational Physics, Institute of Applied Physics and Computational Mathematics, P.O. Box 8009-26, Beijing 100088, China*
[3] *Center for Applied Physics and Technology, MOE Key Center for High Energy Density Physics Simulations, College of Engineering, Peking University, Beijing 100871, China*
*Corresponding authors. E-mail: * shanshiwycf@163.com, † Xu_Aiguo@iapcm.ac.cn*
Received May 8, 2016; accepted June 16, 2016

The two-dimensional Rayleigh–Taylor instability problem is simulated with a multiple-relaxation-time discrete Boltzmann model with a gravity term. Viscosity, heat conductivity, and Prandtl number effects are probed from macroscopic and nonequilibrium viewpoints. In the macro sense, both viscosity and heat conduction show a significant inhibitory effect in the reacceleration stage, which is mainly achieved by inhibiting the development of the Kelvin–Helmholtz instability. Before this, the Prandtl number effect is not sensitive. Viscosity, heat conductivity, and Prandtl number effects on nonequilibrium manifestations and the degree of correlation between the nonuniformity and the nonequilibrium strength in the complex flow are systematically investigated.

Keywords discrete Boltzmann model/method, multiple-relaxation-time, Rayleigh–Taylor instability, nonequilibrium

PACS numbers 47.11.-j, 51.10.+y, 05.20.Dd

1 Introduction

The Rayleigh–Taylor (RT) instability [1, 2] occurs when a heavy fluid lies above a lighter one in a gravitational field with gravity pointing downward. The RT instability can be observed in a wide range of astrophysical and atmospheric flows, and it has great significance in both fundamental research and practical applications. Because of the existence of sharp interfaces and their evolutions, the flow system is out of equilibrium.

Over the decades, many numerical methods have been developed to simulate the RT instability; these include the flux-corrected transport method [3], the level set method [4], the front tracking method [5], the marker-and-cell method [6], the smoothed particle hydrodynamics method [7], the boundary integral method [8], direct numerical simulations [9, 10], large-eddy simulations [11], and the phase-field method [12]. The influences of different factors on the evolution of the RT instability have been studied more and more deeply. Betti *et al.* [13] investigated the effect of vorticity accumulation on the ablative Rayleigh–Taylor instability. Gupta *et al.* [14] investigated the effect of magnetic field, compressibility and density variation on the nonlinear growth rate of the RT instability. Sharma *et al.* [15] analyzed the RT instability of two superposed fluids, taking into account the effect of small rotation, suspended dust particles, and surface tension. Banerjee *et al.* [16] investigated the combined effect of viscosity and vorticity on the growth rate of the bubble associated with single-mode RT instability. To our knowledge, these numerical methods are based on the Euler or Navier–Stokes equations, but Euler and Navier–Stokes models fall short of describing nonequilibrium effects. Consequently, the rich and complex nonequilibrium effects in the RT flow system have been rarely investigated. Meanwhile, molecular dynamic simulations can present helpful information on the nonequilibrium state [17], but owing to the limitation of computer capacity, the spatial and temporal scales it can access are far from large enough.

Besides the numerical methods mentioned above, the Lattice Boltzmann (LB) method [18–29] provides an alternative efficient tool for simulating complex fluid flows, and it has been implemented in the study of the RT instability [30–39]. For instance, Nie *et al.* simulated the

RT instability using a lattice Boltzmann model for multicomponent fluid flows, and Guo *et al.* investigated the effects of the Prandtl number on the mixing process in the RT instability of incompressible and miscible fluids based on a double-distribution-function LB method. Up to now, however, in most of the previous studies this LB method works as a kind of new scheme to solve partial differential equations such as the Euler equations and Navier–Stokes equations.

Recently, some scholars have repositioned the method, regarding it as a kind of new mesoscopic and coarse-grained kinetic model of complex physical systems, which is juxtaposed with the traditional hydrodynamic method. Compared with the first category, this Discrete Boltzmann Method (DBM) possesses kinetic information that is beyond that obtained in a Navier–Stokes approach and brings new physical insights into the physical system. The first DBM description appeared in a review article published in 2012 [40]. In that work, the authors addressed how to investigate both Hydrodynamic NonEquilibrium (HNE) and Thermodynamic NonEquilibrium (TNE) simultaneously in complex flows via the DBM. Subsequently, the DBM has been gradually extended and applied to combustion and detonation systems [41–46], multiphase flow systems [47], and fluid instability systems [48–50]. The finer physical structures of shock waves revealed by the DBM [41–46, 48, 49] have been confirmed and supplemented by the results of nonequilibrium molecular dynamics simulations [17].

In this paper, we present a multiple-relaxation-time (MRT) DBM with gravity. The two-dimensional RT instability problem is simulated, and the results are compared with those in previous studies. The relaxation rates of the various kinetic moments resulting from particle collisions may be adjusted more physically in the MRT version. This overcomes some obvious deficiencies of the Single-Relaxation-Time (SRT) version, such as a fixed Prandtl number. Compared with previous studies on the RT instability, viscosity, heat conductivity, and Prandtl number effects on macro-dynamics and nonequilibrium manifestations are investigated simultaneously in the DBM model. With the increase of viscosity or heat conduction, various nonequilibrium components increase. When the RT instability develops into the turbulent mixing stage, both the global average TNE strength and NonOrganized Energy Flux (NOEF) strength decrease. The degrees of correlation between density nonuniformity and the global average TNE strength and between temperature nonuniformity and global average NOEF strength are numerically probed. The simulation results show that heat conduction plays a major role on the degree of correlation. The modeling of nonequilibrium features is a helpful and effective complement to the macroscopic description. Together, they provide new insights into complex flow systems.

The paper is organized as follows: Section 2 presents the MRT DBM with gravity. Systematic numerical simulations of the RT instability and nonequilibrium characteristics are shown and analyzed in Section 3. A brief conclusion is given in Section 4.

2 Description of the MRT DBM with gravity

The MRT discrete Boltzmann equation with a gravity term reads as follows:

$$\frac{\partial f_i}{\partial t}+v_{i\alpha}\frac{\partial f_i}{\partial x_\alpha}=-\boldsymbol{M}_{il}^{-1}\hat{\boldsymbol{S}}_{lk}(\hat{f}_k-\hat{f}_k^{eq})-g_\alpha\frac{(v_{i\alpha}-u_\alpha)}{RT}f_i^{eq}, \tag{1}$$

where $\boldsymbol{v}_i$ is the discrete particle velocity, $i=1,\ldots,N$, and N is the number of discrete velocities. The matrix $\hat{\boldsymbol{S}}=\mathrm{diag}(s_1,s_2,\cdots,s_N)$ is the diagonal relaxation matrix. f_i and $\hat{f}_i$ (f_i^{eq} and $\hat{f}_i^{eq}$) are the particle (equilibrium) distribution functions in velocity space and kinetic moment space, respectively; the mapping between moment space and velocity space is defined by the linear transformation M_{ij}, i.e., $\hat{f}_i=M_{ij}f_j$ and $f_i=M_{ij}^{-1}\hat{f}_j$. g_α is the acceleration, u_α is the macroscopic velocity, and T is the temperature.

Chapman–Enskog analysis indicates that it is independent of the Discrete Velocity Model (DVM). Therefore, choosing the DVM provides us with high flexibility. Here, the following two-dimensional discrete velocity model is used:

$$(v_{i1},v_{i2})=\begin{cases}\textbf{cyc}:c\,(\pm1,0)\,, & \text{for } 1\le i\le 4,\\ c\,(\pm1,\pm1)\,, & \text{for } 5\le i\le 8,\\ \textbf{cyc}:2c\,(\pm1,0)\,, & \text{for } 9\le i\le 12,\\ 2c\,(\pm1,\pm1)\,, & \text{for } 13\le i\le 16,\end{cases} \tag{2}$$

where **cyc** indicates cyclic permutation, $\eta_i=\eta_0$ for $i=1,\ldots,4$, and $\eta_i=0$ for $i=5,\ldots,16$.

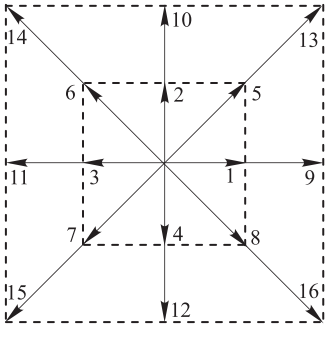

Fig. 1 Schematic of the discrete-velocity model.

The transformation matrix and the corresponding equilibrium distribution functions in kinetic moment space (KMS) are constructed according to the seven moment relations. Specifically, the transformation matrix is $\boldsymbol{M} = (m_1, m_2, \cdots, m_{16})^T, m_i = (1, v_{ix}, v_{iy}, (v_{i\alpha}^2 + \eta_i^2)/2, v_{ix}^2, v_{ix}v_{iy}, v_{iy}^2, (v_{i\beta}^2 + \eta_i^2)v_{ix}/2, (v_{i\beta}^2 + \eta_i^2)v_{iy}/2, v_{ix}^3, v_{ix}^2 v_{iy}, v_{ix}v_{iy}^2, v_{iy}^3, (v_{i\chi}^2 + \eta_i^2)v_{ix}^2/2, (v_{i\chi}^2 + \eta_i^2)v_{ix}v_{iy}/2, (v_{i\chi}^2 + \eta_i^2)v_{iy}^2/2)$. The corresponding equilibrium distribution functions in KMS are $\hat{f}_1^{eq} = \rho$, $\hat{f}_2^{eq} = j_x$, $\hat{f}_3^{eq} = j_y$, $\hat{f}_4^{eq} = e$, $\hat{f}_5^{eq} = P + \rho u_x^2$, $\hat{f}_6^{eq} = \rho u_x u_y$, $\hat{f}_7^{eq} = P + \rho u_y^2$, $\hat{f}_8^{eq} = (e + P)u_x$, $\hat{f}_9^{eq} = (e + P)u_y$, $\hat{f}_{10}^{eq} = \rho u_x(3T + u_x^2)$, $\hat{f}_{11}^{eq} = \rho u_y(T + u_x^2)$, $\hat{f}_{12}^{eq} = \rho u_x(T + u_y^2)$, $\hat{f}_{13}^{eq} = \rho u_y(3T + u_y^2)$, $\hat{f}_{14}^{eq} = (e+P)T+(e+2P)u_x^2$, $\hat{f}_{15}^{eq} = (e+2P)u_x u_y$, and $\hat{f}_{16}^{eq} = (e + P)T + (e + 2P)u_y^2$, where pressure $P = \rho RT$ and energy $e = b\rho RT/2 + \rho u_\alpha^2/2$.

By using the Chapman–Enskog expansion on the two sides of the discrete Boltzmann equation (see the Appendix for details), the final Navier–Stokes equations with a gravity term for both compressible fluids and incompressible fluids can be obtained:

$$\frac{\partial \rho}{\partial t} + \frac{\partial(\rho u_\alpha)}{\partial x_\alpha} = 0, \tag{3a}$$

$$\frac{\partial(\rho u_\alpha)}{\partial t} + \frac{\partial(\rho u_\alpha u_\beta)}{\partial x_\beta} + \frac{\partial P}{\partial x_\alpha} = \frac{\partial}{\partial x_\beta}\left[\mu\left(\frac{\partial u_\alpha}{\partial x_\beta} + \frac{\partial u_\beta}{\partial x_\alpha} - \frac{2}{b}\frac{\partial u_\chi}{\partial x_\chi}\delta_{\alpha\beta}\right)\right] - \rho g_\alpha, \tag{3b}$$

$$\frac{\partial e}{\partial t} + \frac{\partial}{\partial x_\alpha}[(e + P)u_\alpha] = \frac{\partial}{\partial x_\beta}\left[\lambda\frac{\partial T}{\partial x_\beta} + \mu\left(\frac{\partial u_\alpha}{\partial x_\beta} + \frac{\partial u_\beta}{\partial x_\alpha} - \frac{2}{b}\frac{\partial u_\chi}{\partial x_\chi}\delta_{\alpha\beta}\right)u_\alpha\right] - \rho g_\alpha u_\alpha, \tag{3c}$$

where $\alpha, \beta, \chi = x, y$, the viscosity $\mu = \rho RT/s_v$ ($s_v = s_5 = s_6 = s_7$), and the heat conductivity $\lambda = (\frac{b}{2} + 1)\rho R^2 T/s_T$ ($s_T = s_8 = s_9$).

3 Numerical Simulations

3.1 Performance on a discontinuity

To check the performance of the difference scheme on a discontinuity, we construct the following problem:

$$\begin{cases} (\rho, u_1, u_2, T) = (1.71429, 0.0, 0.697217, 1.26389), \\ \qquad\qquad y \le L/2, \\ (\rho, u_1, u_2, T) = (1.0, 0.0, 0.0, 1.0), \\ \qquad\qquad L/2 < y \le L, \end{cases} \tag{4}$$

where L is the length of the computational domain. The physical quantities on the two sides satisfy the Hugoniot relations, and the specific heat ratio $\gamma = 1.4$. In the y direction $f_i = \boldsymbol{M}_{ij}^{-1}\hat{f}_j^{eq}$, and the macroscopic quantities adopt the initial values. In the x direction, the periodic boundary condition is adopted. Figure 2 shows the simulation results of density at time $t = 12$ using different space discretization schemes. The parameters are $c = 2$, $\eta_0 = 4$, $\mathrm{d}x = \mathrm{d}y = 0.2$, $\mathrm{d}t = 10^{-4}$, and $s_i = 10^4$, $i = 1, \ldots, 16$. Simulations with a Lax–Wendroff scheme have strong unphysical oscillations in the shocked region. The second- order upwind scheme results in unphysical overshoot phenomena at the shock front. The simulation result with the WENO scheme is much more accurate and decreases the unphysical oscillations at the discontinuity.

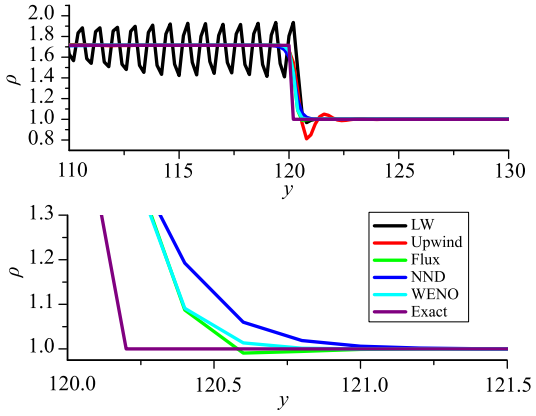

Fig. 2 Density profiles with various difference schemes at $t = 12$.

3.2 Macro-characteristics of the Rayleigh–Taylor instability

In this section, we describe numerical simulations of the RT instability. The computational domain is a two-dimensional box with height $H = 80$ and width $W = 20$, and the initial hydrostatic unstable configuration is given by

$$\begin{cases} T_0(y) = T_u,\ \rho_0(y) = \rho_u \exp(-g(y - y_s)/T_u), & y \ge y_s, \\ T_0(y) = T_b,\ \rho_0(y) = \rho_b \exp(-g(y - y_s)/T_b), & y < y_s, \end{cases} \tag{5}$$

where $y_s = 40 + 2\cos(0.1\pi x)$ is the initial small perturbation at the interface. To be at equilibrium, the same pressure at the interface should be required:

$$p_0 = \rho_u T_u = \rho_b T_b, \tag{6}$$

where $T_u < T_b$ and $\rho_u > \rho_b$. To have a finite width of the initial interface, all numerical experiments are performed by preparing the initial configuration plus a smooth interpolation between the two half-volumes. The initial

temperature profile is therefore chosen to be

$$T_0(y) = (T_u+T_b)/2+(T_u-T_b)/2\times\tanh((y-y_s)/w), \quad (7)$$

where w denotes the initial width of the interface. The initial density $\rho_0(y)$ is then fixed by the initial settings [Eqs. (5)–(6)] combined with the smoothed temperature profile. In the simulation, the bottom is solid, the top is free (that is, an outflow condition), and the left and right boundaries are periodic boundary conditions. The fifth-order WENO scheme is used for space discretization, while time evolution is performed through the third-order Runge-Kutta scheme.

To verify the validity of the calculation, a grid convergence study is conducted using different grids: $Nx \times Ny = 100 \times 400$ (grid I) and $Nx \times Ny = 200 \times 800$ (grid II). The initial conditions are $\rho_b = 1$, $T_b = 1.4$, $\rho_u = 2.33333$, $T_u = 0.6$, $g_x = 0$, $g_y = 0.005$, $w = 0.8$, $\gamma = 1.4$, and Atwood number $A = 0.4$. Figure 3 shows the density and temperature distributions along the line $x = 5$ at time $t = 200$, where $c = 1$, $\eta_0 = 3$, $dt = 10^{-3}$, and all of the collision parameters are 10^3. As one can see, the agreement is good, and grid I is sufficient for simulating the RT problem.

Figure 4 shows the evolution of the fluid interface at times $t = 0$, 100, 200, 300, and 400. The bubble amplitude, spike amplitude, bubble growth rate, and spike growth rate can be seen in Fig. 5, where they are represented by the black lines. When the amplitude of the perturbation is much smaller than the wavelength, the perturbation of the fluid interface experiences exponential growth. In the spike formation stage, the heavy and light fluids gradually penetrate into each other as time progresses, with the light fluid rising to form a bubble and the heavy fluid falling to generate a spike. The interface becomes more acute and the growth rate increases approximately linearly. Subsequently, the Kelvin–Helmholtz instability begins to develop and this leads to the accumulation of heavy fluid at the top of the spike. The interface gradually becomes blunt, even forming eddies under certain conditions. The spike growth rate is reduced, and the bubble growth rate reaches a constant velocity after a small attenuation. This is the nonlinear stage. Taylor derived an empirical formula for the constant velocity: $v_b = C\sqrt{AgW/2}$, where $C = 0.32$. In the simulation, the fitting constant speed of the bubble is 0.05329, so $C = 0.3768$. The difference is due to the free condition at the top. In a test with a solid wall condition at the top, the fitting constant velocity is 0.04622, and $C = 0.3268$. This agrees well with Taylor and Layzer's results [51]. At a later time, extrusion

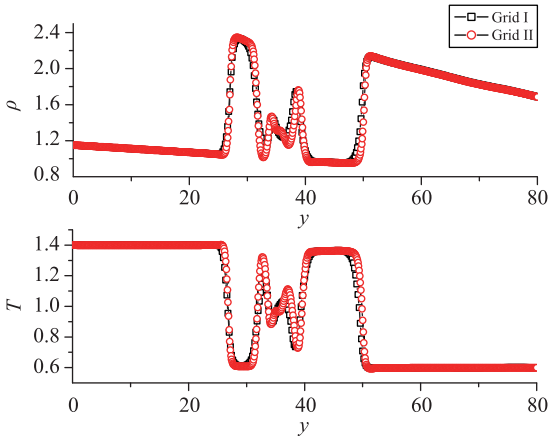

Fig. 3 Grid convergence study: density and temperature profiles at the line $x = 5$ at time $t = 200$.

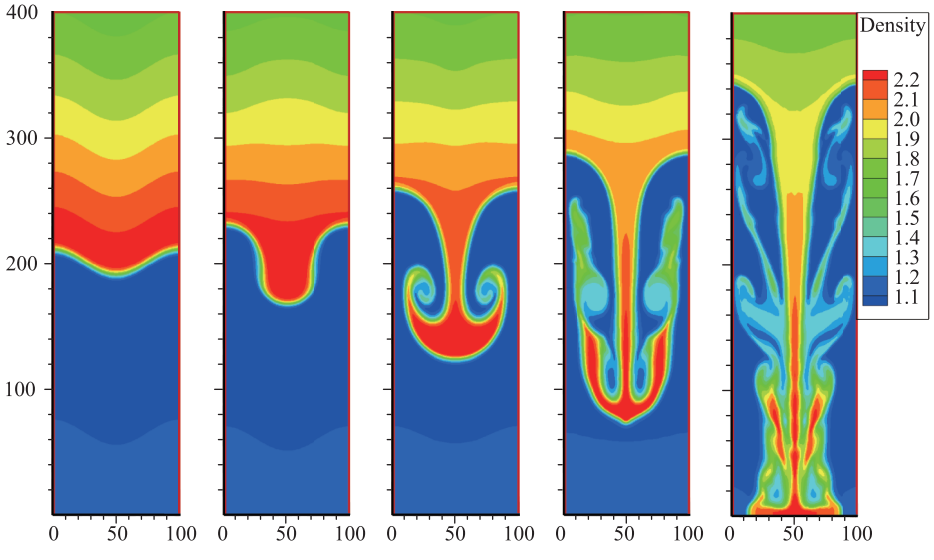

Fig. 4 Evolution of the fluid interface from a single-mode perturbation.

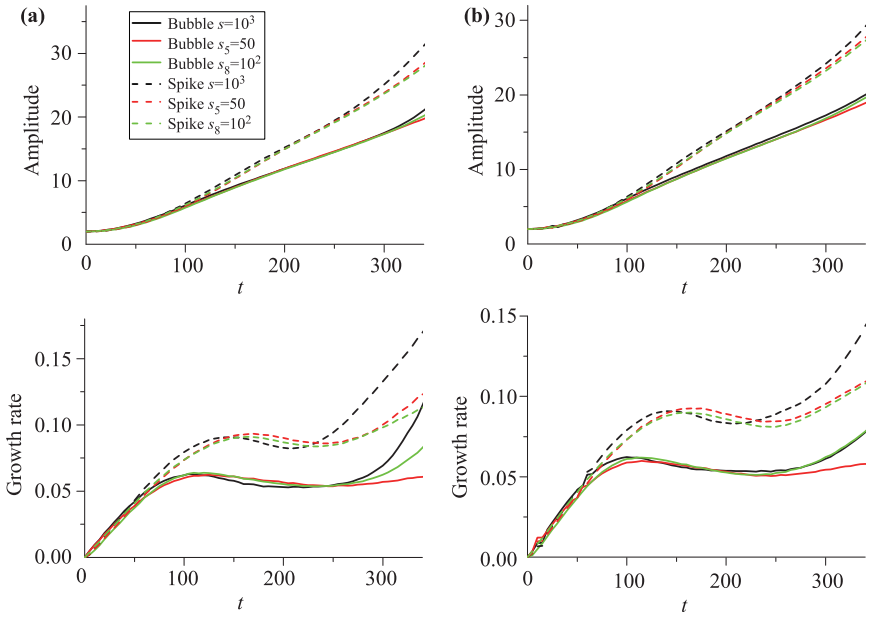

Fig. 5 Amplitude and growth rate with different viscosities or thermal conductivities. **(a)** $\gamma = 1.4$; **(b)** $\gamma = 1.667$.

from the two sides leads to the formation of secondary spikes, and the growth rate increases again (reacceleration stage). The shapes of the fluid interface in the current study compare well with those in previous studies [31, 52]. The amplitude of the spike is greater than that of the bubble, and the ratio is changing with time. After full development of the interface, the ratio is between 1.5 and 1.7, which is consistent with the numerical results of Youngs [53].

Figure 6 shows the vertical distribution curve of the heavy fluid, $m(y)$, at different times, which is defined as

$$m(y) = \sum_{ix=1}^{Nx} \rho(\mathrm{i}x, \mathrm{i}y)/(NX). \tag{8}$$

The occurrence and growth of the peak value of the heavy fluid vertical distribution at time $t = 150$, and 200, represent the accumulation of heavy fluid at the tip of the spike. Under the extrusion action from the two sides, the interface along the two vortices is stretched, the peak value of the heavy fluid vertical distribution decreases gradually, and the distribution tends to be approximately an equilibrium one.

The effects of viscosity and thermal conductivity on the RT instability are also shown in Figs. 5(a) (for $\gamma = 1.4$) and (b) (for $\gamma = 1.667$). The black curves correspond to simulation results of $s = 10^3$ ($Pr = 1$), the red curves correspond to simulation results of $s_v = 50$ (with other collision parameters being 10^3 and $Pr = 20$), and the green curves correspond to $s_T = 10^2$ (with other collision parameters being 10^3 and $Pr = 0.1$). Solid and dotted lines denote bubbles and spikes, respectively. Before entering the reacceleration stage, the effects of viscosity and thermal conductivity on the RT instability are negligible. During the reacceleration stage, both viscosity and thermal conductivity show a significant inhibitory effect. In Fig. 7, we can find the explanation for this. Figures 7(a), (b), and (c) correspond to $Pr = 20$, $Pr = 1$, and $Pr = 0.1$, respectively. With the decrease of s_v or s_T, the viscosity or thermal conductivity increases, the complicated secondary vortices generated by the Kelvin–Helmholtz instability are suppressed, and then the evolution of the RT instability is suppressed. That is, the inhibition effect of viscosity and thermal conductivity on the RT instability is mainly achieved by inhibiting the development of the Kelvin–Helmholtz instability in the RT instability.

3.3 Nonequilibrium characteristics of the Rayleigh–Taylor instability

In the MRT model, the deviation from equilibrium can be defined as $\Delta_i = \hat{f}_i - \hat{f}_i^{eq} = \boldsymbol{M}_{ij}(f_j - f_j^{eq})$. Δ_i contains the information of the macroscopic flow velocity u_α. Furthermore, we replace $v_{i\alpha}$ by $v_{i\alpha} - u_\alpha$ in the transformation matrix $\boldsymbol{M}$, named $\boldsymbol{M}^*$. $\Delta_i^* = \boldsymbol{M}_{ij}^*(f_j - f_j^{eq})$ is only the manifestation of molecular thermal motion and does not contain the information of the macroscopic flow. To clarify the meaning of Δ_i^*, we introduce the notation $\Delta_{2xx}^* = \Delta_5^*$, $\Delta_{2xy}^* = \Delta_6^*$, $\Delta_{2yy}^* = \Delta_7^*$, $\Delta_{(3,1)x}^* = \Delta_8^*$, $\Delta_{(3,1)y}^* = \Delta_9^*$, $\Delta_{3xxx}^* = \Delta_{10}^*$, $\Delta_{3xxy}^* = \Delta_{11}^*$, $\Delta_{3xyy}^* = \Delta_{12}^*$, $\Delta_{3yyy}^* = \Delta_{13}^*$, $\Delta_{(4,2)xx}^* = \Delta_{14}^*$, $\Delta_{(4,2)xy}^* = \Delta_{15}^*$, and $\Delta_{(4,2)yy}^* = \Delta_{16}^*$. Here Δ_{2xx}^* and Δ_{2yy}^* describe the departures of the internal energies in the x and y degrees

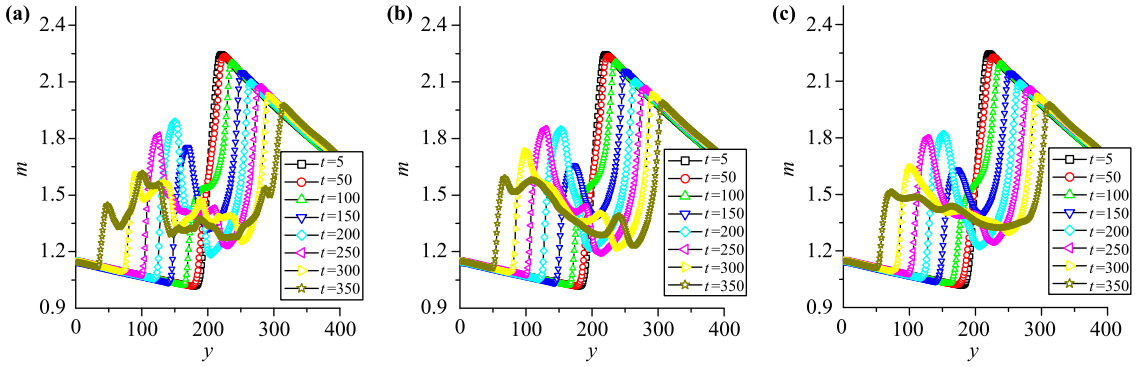

Fig. 6 Evolution of the heavy material vertical distribution curve.

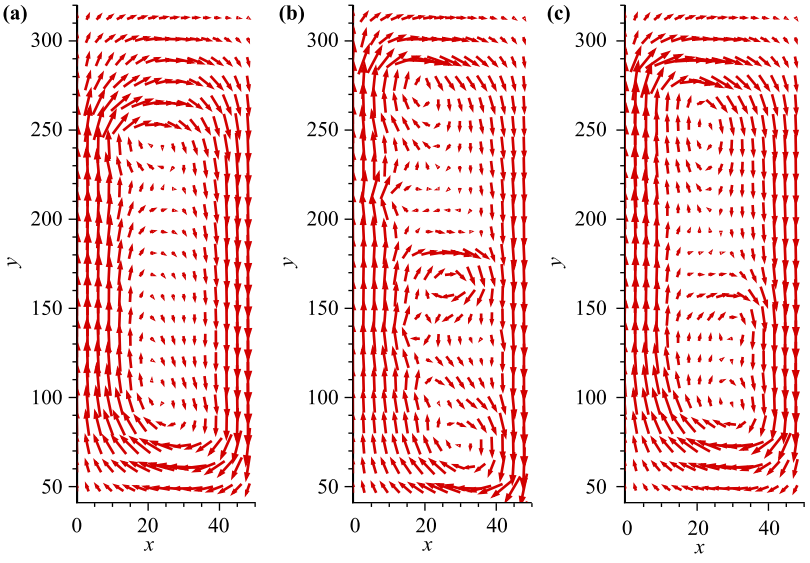

Fig. 7 Velocity vector plots of the RT instability ($\gamma = 1.4$) in $[0, 50] \times [41, 320]$ at time $t = 350$, showing **(a)** $s_v = 50$, **(b)** $s = 10^3$, and **(c)** $s_T = 10^2$.

of freedom from their average; Δ^*_{2xy} denotes shear effects; Δ^*_{3xxx}, Δ^*_{3xyy}, and $\Delta^*_{(3,1)x}$ are related to the internal energy flow caused by microscopic fluctuations in the x direction; and Δ^*_{3xxy}, Δ^*_{3yyy}, and $\Delta^*_{(3,1)y}$ are associated with the internal energy flow caused by microscopic fluctuation in the y direction. Compared with the macroscopic equations, $\Delta^*_{2\alpha\beta}$ and $\Delta^*_{(3,1)\alpha}$ correspond to the viscous stress tensor in the momentum equation and the heat flux term in the energy equation, which are referred to as NonOrganized Momentum Flux (NOMF) and NOEF, respectively [54].

To provide a rough estimation of TNE, we follow the idea used in Refs. [43] and define a nondimensional "TNE strength" function

$$d(x,y) = \sqrt{\frac{\Delta^{*2}_{2\alpha\beta}}{T^2} + \frac{\Delta^{*2}_{(3,1)\alpha}}{T^3} + \frac{\Delta^{*2}_{3\alpha\beta\gamma}}{T^3} + \frac{\Delta^{*2}_{(4,2)\alpha}}{T^4}},$$

where $d = 0$ in the thermodynamic equilibrium state and $d > 0$ in the thermodynamic nonequilibrium state. $D_{TNE} = \overline{d}$ is the global average TNE strength. Then we define $D_2 = \sqrt{\overline{\Delta^{*2}_{2\alpha\beta}}}$ and $D_{(3,1)} = \sqrt{\overline{\Delta^{*2}_{(3,1)\alpha}}}$, where D_2 and $D_{(3,1)}$ are the global average NOMF strength and NOEF strength, respectively. Correspondingly, a macroscopic nonuniformity function is defined as

$$\delta W(x,y) = \sqrt{\overline{(W - \overline{W})^2}},$$

where $W = (\rho, U, T)$ denotes the macroscopic distribution and $\overline{W}$ is the average value of a small cell around the point (x, y).

Here we first give some results for Δ^*_i in the evolution of the RT instability. The initial physical quantities (ρ, T, u_x, u_y) are given the same values as those in Fig. 4. Figure 8 shows the simulation results of physical quantities and their gradients in the line $x = 10$ at time $t = 225$. Figure 9 shows the nonequilibrium characteristics of the RT instability with different values of viscosity or heat

conduction. The first line corresponds to $s = 10^3$ (case I), the second line corresponds to $s = 10^2$ (case II), the third line corresponds to $s_v = 10^2$ (case III), and the fourth line corresponds to $s_T = 10^2$ (with other collision parameters being 10^3) (case IV). A vertical dashed line is plotted in each panel to guide the eye for the peak of the spike. From Figs. 8 and 9, we can get the following information:

1) $\Delta^*_{2xx,2yy,(3,1)y,3xxy,3yyy}$ in case II, $\Delta^*_{2xx,2yy}$ in case III, and $\Delta^*_{(3,1)y}$ in case IV are much larger than the values in case I. This is because the relaxation time needed to recover balance is inversely proportional to s_i. As s_i decreases, the corresponding mode will take more time to restore equilibrium, and the degree of deviation from equilibrium increases. Physically, the viscosity and heat conductivity of the physical system in case II, the vis-

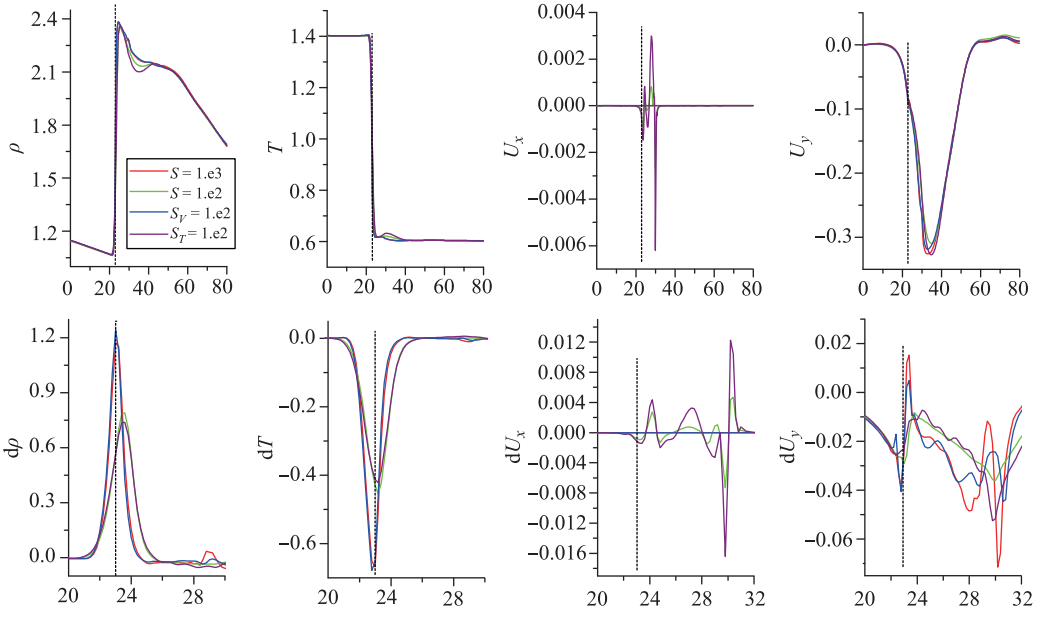

Fig. 8 Physical quantities and their gradients in the line $x = 10$ at time $t = 225$.

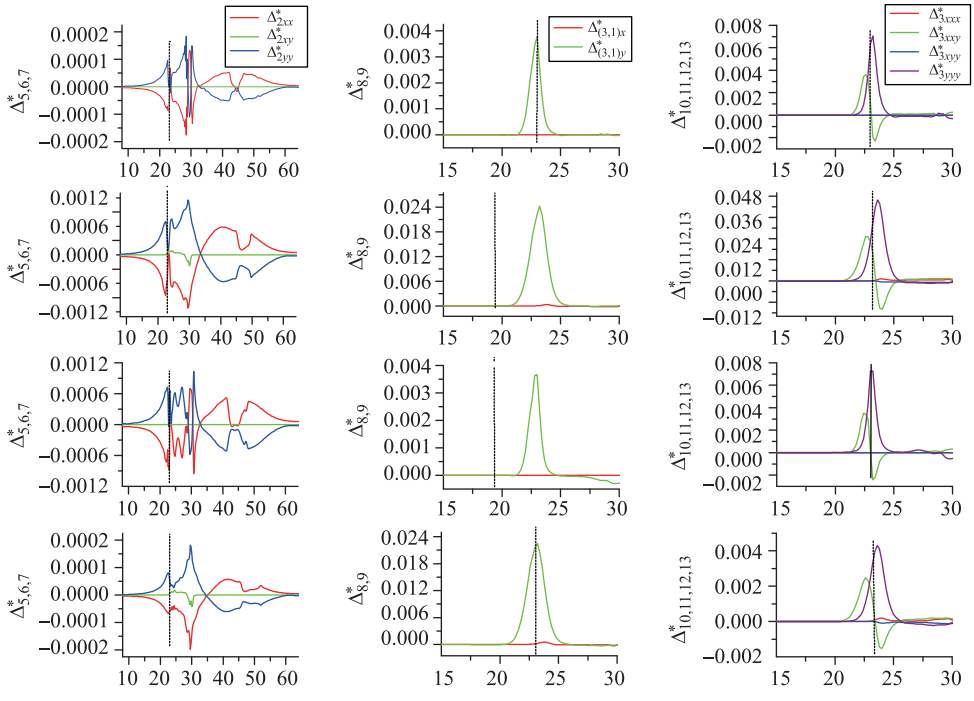

Fig. 9 Nonequilibrium characteristics in the line $x = 10$ at time $t = 225$ in four cases.

cosity in case III, and the heat conductivity in case IV are larger than the values in case I, which increases the nonequilibrium behavior of the system.

2) $\Delta^*_{(3,1)x,(3,1)y,3xxx,3xxy,3xyy,3yyy}$ in case III are similar to the values of case I and $\Delta^*_{2xx,2yy,3xxy,3yyy}$ in case IV are smaller than the values of case I. This can be explained as follows: The relaxation parameters s_i ($i = 8, 9, 10, 11, 12, 13$), density gradient, and temperature gradient in case III are consistent with those in case I. The relaxation parameters s_i ($i = 5, 7, 11, 13$) in case IV are the same as those in case I, but the larger heat conductivity leads to a decrease in the density and temperature gradients, which reduces the nonequilibrium effect. There is a competition among the viscosity, heat conduction, and the gradient of physical quantities.

3) $\Delta^*_{2xy,(3,1)x,3xxx,3xyy}$ in cases I and III are equal to zero, but the values in cases II and IV are not equal to zero. The reason for this is that there is neither a shear effect nor an energy flux in the x direction in cases I and III ($u_x = 0$), so $\Delta^*_{2xy,(3,1)x,3xxx,3xyy} = 0$. In cases II and IV, the opposite occurs.

Figure 10 shows viscosity, heat conductivity, and Prandtl number effects on the global average nonequilibrium characteristics for $Pr = 0.5$ [Fig. 10(a)], $Pr = 1.0$ [Fig. 10(b)], and $Pr = 2.0$ [Fig. 10(c)]. With the increase of viscosity and heat conduction, D_{TNE}, D_2, and $D_{(3,1)}$ will all increase. The change of TNE strength is more significant when heat conduction changes. The growth of D_2 and $D_{(3,1)}$ depends on the viscosity and thermal conductivity, respectively. This further proves the correspondence between $\Delta^*_{2\alpha\beta}$ and the viscosity term and the correspondence between $\Delta^*_{(3,1)\alpha}$ and the heat conduction term in the Navier–Stokes equation. When the spike arrives at the bottom of the calculation domain, or the RT instability develops into the turbulent mixing stage, the global average TNE strength and NOEF strength begin to decrease, and the global average NOMF strength growth slows. The inclined dashed lines roughly show the time at which spikes reach the bottom boundary of the calculation domain. When the viscosity and heat conduction are relatively small, the spike develops relatively quickly and reaches the bottom earlier. This is consistent with the previous conclusion.

Figure 11 shows snapshots of the density nonuniformity $\delta\rho$ and the TNE strength d at times $t = 200$ and $t = 400$. $\delta\rho$ and d demonstrate the HNE and TNE behaviors of the system, respectively. In the position far from the perturbation interface, $\delta\rho$ and d are basically 0. Around the interface, particles with different density mix with each other, producing exchanges of kinetic energy and momentum, and $\delta\rho$ and d are greater than zero. The characteristics of density nonuniformity $\delta\rho$ and TNE strength d are quite consistent. HNE and TNE are thus interrelated. In addition, both $\delta\rho$ and d can be used to

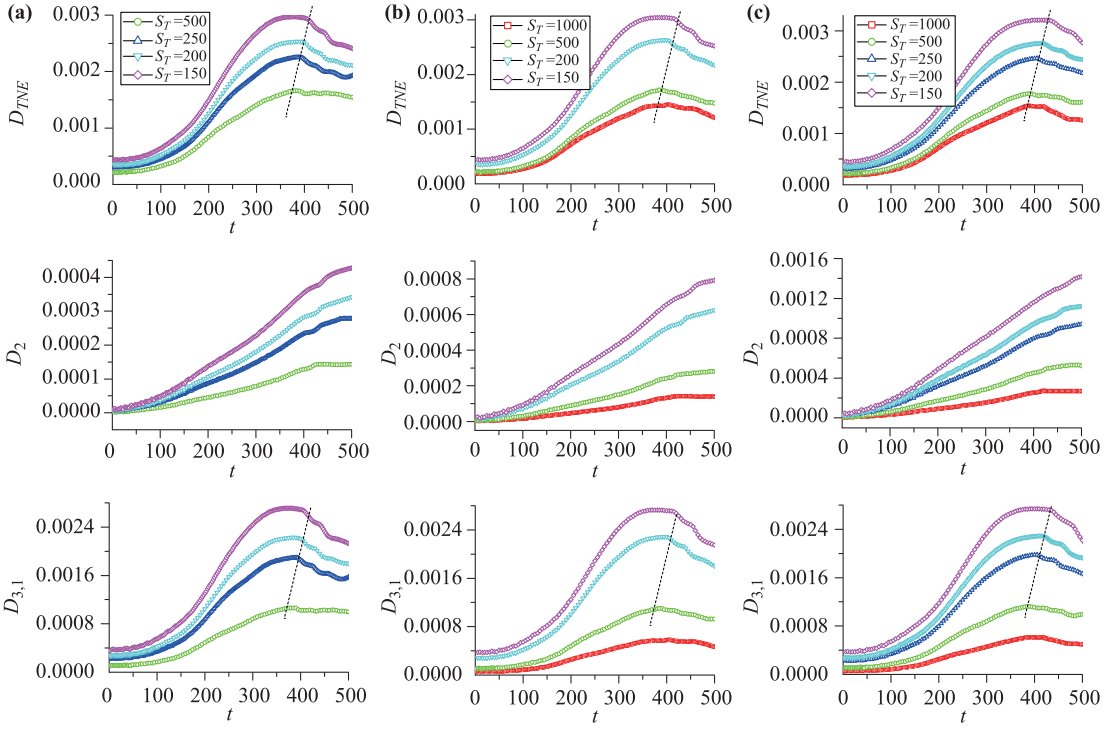

Fig. 10 Prandtl number effects on the global average nonequilibrium characteristics: **(a)** $Pr = 0.5$, **(b)** $Pr = 1.0$, and **(c)** $Pr = 2.0$.

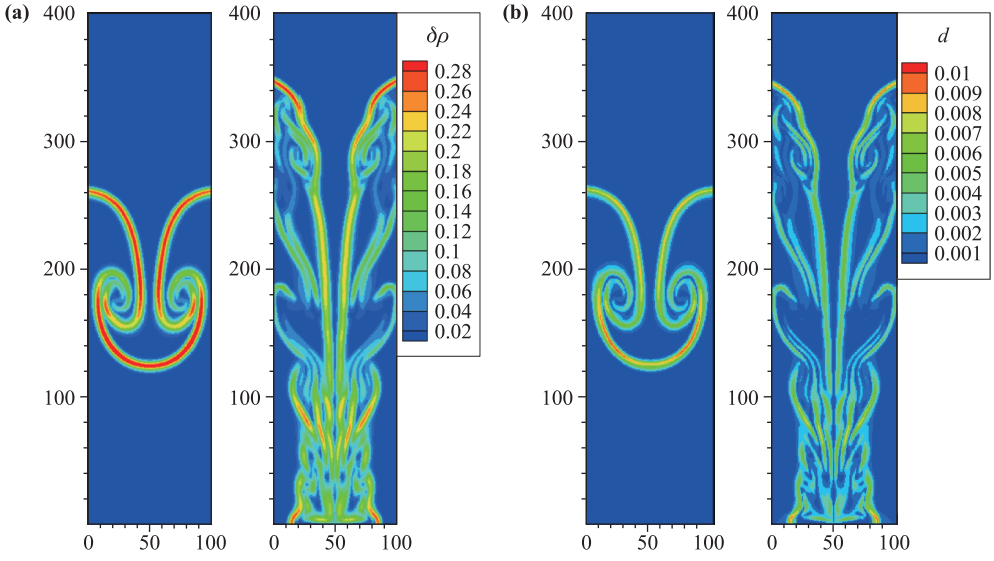

Fig. 11 Snapshots of density nonuniformity $\delta\rho$ **(a)** and TNE strength d **(b)** at times $t = 200$ and $t = 400$.

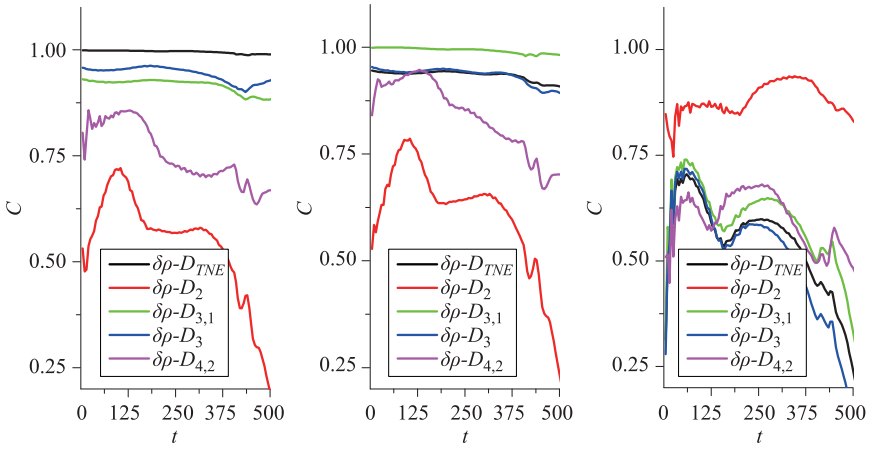

Fig. 12 Degrees of correlation between the macroscopic nonuniformities and various global average nonequilibrium strength values. $\delta\rho$, δT, and δU are density nonuniformity, temperature nonuniformity, and velocity nonuniformity, respectively.

capture the interface.

Figure 12 shows the degrees of correlation between macroscopic nonuniformities and various global average nonequilibrium strength values in the case of $s_v = 300$, $s_T = 150$. In the figure, considerably higher degrees of correlation are found between the density nonuniformity and the global average TNE strength D_{TNE} and between the temperature nonuniformity and the global average NOEF strength $D_{(3,1)}$, both of which are approximately 1. The degree of correlation between the velocity nonuniformity and the global average NOMF strength D_2 is higher than that with other nonequilibrium strength values.

In Fig. 13(a), we can see that the degree of correlation between $\delta\rho$ and D_{TNE} varies with viscosity and heat conduction. Before the turbulent mixing stage, heat conduction plays a major role. The greater the heat conduction, the higher the degree of correlation. With the increase of heat conduction, the degree of correlation gradually tends to 1 [Fig. 13(b)]. The trend can be expressed by an exponential decay function [Fig. 13(c)],

$$C_{\delta\rho\text{-}D_{TNE}} = 1 - 0.102\exp(-H_{2b} \times 10^5/5.22),$$
$$H_{2b} = \sqrt{gk}/s_T, \tag{9}$$

where H_{2b} is the relative thermal conductivity and k is the wave number. The effect of viscosity is reflected in the turbulent mixing stage, When heat conduction is constant, the higher the viscosity is, the higher the degree of correlation. When the degree of correlation between functions A and B is equal to 1, there is a linear relationship between A and B; that is, $B = \alpha A + \beta$. Figure 13(d) shows the linear relationship between $\delta\rho$ and D_{TNE}. The

solid lines are the fitted curves. As can be seen in the figure, the slope α of the linear relationship is determined by the heat conduction: $\alpha_1 = 0.025 + 240 \times H_{2b}$.

In Fig. 14, we can see that the degree of correlation between δT and the global average NOEF strength $D_{(3,1)}$ also varies with both viscosity and heat conduction. Before time $t = 200$, heat conduction plays a major role. The greater the heat conduction, the higher the degree of correlation. The effect of viscosity in the nonlinear stage is more obvious than in the linear stage. A

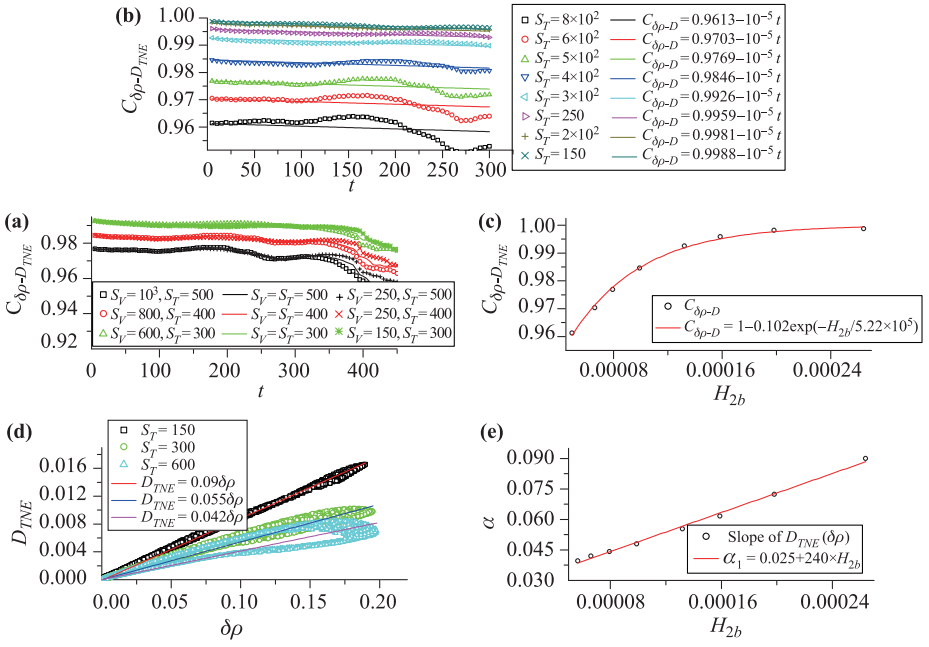

Fig. 13 Degree of correlation between $\delta\rho$ and D_{TNE}: **(a)** Effects of viscosity and heat conduction, **(b)** and **(c)** Variation of correlation degree with heat conduction, **(d)** Linear relationship between $\delta\rho$ and D_{TNE}, and **(e)** Slope α of the linear relationship.

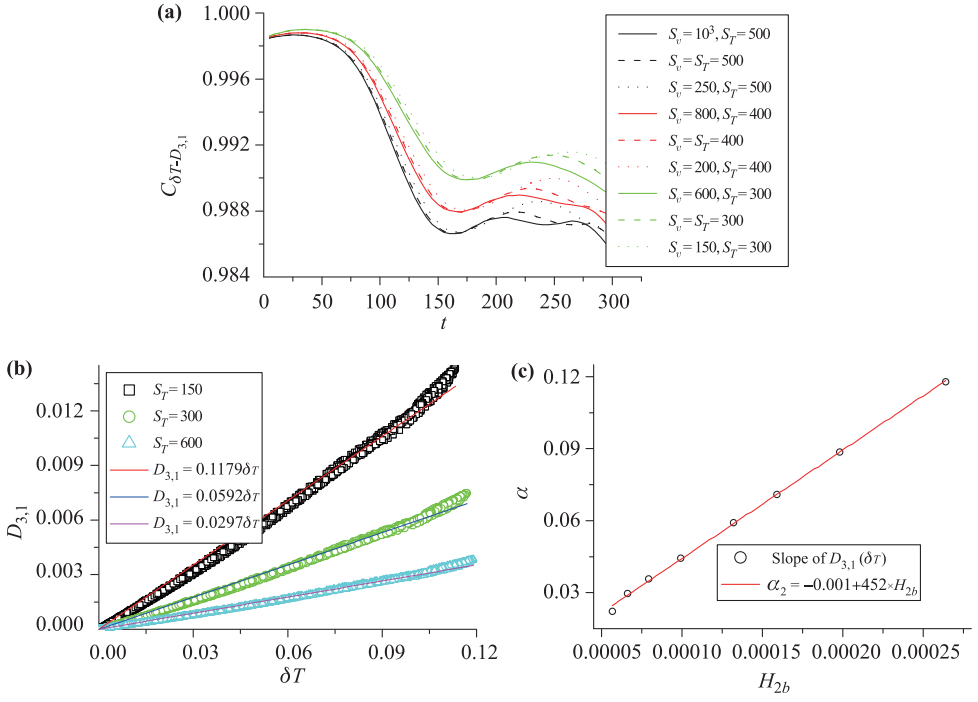

Fig. 14 Degree of correlation between δT and $D_{(3,1)}$: **(a)** Effect of viscosity and heat conduction, **(b)** Linear relationship between δT and $D_{(3,1)}$, and **(c)** Slope α of the linear relationship.

linear relationship between δT and $D_{(3,1)}$ is also found, and the slope is also determined by the heat conduction: $\alpha_2 = -0.001 + 452 \times H_{2b}$.

4 Conclusions

With an MRT discrete Boltzmann model, the two-dimensional Rayleigh–Taylor instability with different viscosity, thermal conductivity, and Prandtl number values is simulated. Both viscosity and heat conduction show a significant inhibitory effect on the RT instability, which is mainly achieved by inhibiting the development of the Kelvin–Helmholtz instability during the reacceleration stage. Before this, the Prandtl number effect is not sensitive. Nonequilibrium characteristics of the system are mainly probed. With the increase of viscosity or heat conduction, different nonequilibrium components increase. There is a competition among the viscosity, heat conduction, and the gradient of physical quantities. When the RT instability develops into the turbulent mixing stage, both the global average TNE strength and the NOEF strength decrease. The degrees of correlation between macroscopic nonuniformities and various global average nonequilibrium strength values are analyzed. The degrees of correlation between the density nonuniformity and the global average TNE strength and between the temperature nonuniformity and the global average NOEF strength are both approximately 1. Heat conduction plays a major role in the degree of correlation.

Acknowledgements F.C. acknowledges support from the National Natural Science Foundation of China (Grant No. 11402138). A.X. and G.Z. acknowledge support from the Foundation of LCP and the National Natural Science Foundation of China (Grant No. 11475028).

Appendix A CE expansion for the MRT DBM with gravity

By using the Chapman–Enskog expansion on both sides of the discrete Boltzmann equation, the Navier–Stokes equations with a gravity term can be derived.

We define

$$\frac{\partial f_i}{\partial t} + v_{i\alpha}\frac{\partial f_i}{\partial x_\alpha} = -\boldsymbol{S}_{il}\left(f_l - f_l^{eq}\right) - f_i^F, \tag{A1a}$$

$$f_i = f_i^{(0)} + f_i^{(1)} + f_i^{(2)}, \tag{A1b}$$

$$\frac{\partial}{\partial t} = \frac{\partial}{\partial t_1} + \frac{\partial}{\partial t_2}, \tag{A1c}$$

$$\frac{\partial}{\partial x} = \frac{\partial}{\partial x_1}, \tag{A1d}$$

where $f_i^F = g_\alpha \frac{(v_{i\alpha}-u_\alpha)}{RT} f_i^{eq}$, with nonequilibrium parts $f_i^{(l)} = O(\epsilon^l)$ and partial derivatives $\partial/\partial t_l = O(\epsilon^l)$ and $\partial/\partial x_l = O(\epsilon^l)$ $(l = 1, 2, \ldots)$. Equating coefficients of the zeroth-, first-, and the second-order terms in ϵ gives

$$f_i^{(0)} = f_i^{eq}, \tag{A2a}$$

$$\left(\frac{\partial}{\partial t_1} + v_{i\alpha}\frac{\partial}{\partial x_{1\alpha}}\right) f_i^{(0)} = -\boldsymbol{S}_{il} f_l^{(1)} - f_i^F, \tag{A2b}$$

$$\frac{\partial}{\partial t_2} f_i^{(0)} + \left(\frac{\partial}{\partial t_1} + v_{i\alpha}\frac{\partial}{\partial x_{1\alpha}}\right) f_i^{(1)} = -\boldsymbol{S}_{il} f_l^{(2)}. \tag{A2c}$$

These can be converted into moment space to obtain

$$\hat{\boldsymbol{f}}^{(0)} = \hat{\boldsymbol{f}}^{eq}, \tag{A3a}$$

$$\left(\frac{\partial}{\partial t_1} + \hat{\boldsymbol{E}}_\alpha\frac{\partial}{\partial x_{1\alpha}}\right) \hat{\boldsymbol{f}}^{(0)} = -\hat{\boldsymbol{S}}\hat{\boldsymbol{f}}^{(1)} - \hat{\boldsymbol{f}}^F, \tag{A3b}$$

$$\frac{\partial}{\partial t_2}\hat{\boldsymbol{f}}^{(0)} + \left(\frac{\partial}{\partial t_1} + \hat{\boldsymbol{E}}_\alpha\frac{\partial}{\partial x_{1\alpha}}\right) \hat{\boldsymbol{f}}^{(1)} = -\hat{\boldsymbol{S}}\hat{\boldsymbol{f}}^{(2)}, \tag{A3c}$$

where $\hat{\boldsymbol{E}}_\alpha = \boldsymbol{M}(v_{i\alpha}\boldsymbol{I})\boldsymbol{M}^{-1}$.

From Eq. (A3b), we obtain

$$\frac{\partial}{\partial t_1}\hat{f}_1^{eq} + \frac{\partial}{\partial x_1}\hat{f}_2^{eq} + \frac{\partial}{\partial y_1}\hat{f}_3^{eq} = -\hat{f}_1^F, \tag{A4a}$$

$$\frac{\partial}{\partial t_1}\hat{f}_2^{eq} + \frac{\partial}{\partial x_1}\hat{f}_5^{eq} + \frac{\partial}{\partial y_1}\hat{f}_6^{eq} = -\hat{f}_2^F, \tag{A4b}$$

$$\frac{\partial}{\partial t_1}\hat{f}_3^{eq} + \frac{\partial}{\partial x_1}\hat{f}_6^{eq} + \frac{\partial}{\partial y_1}\hat{f}_7^{eq} = -\hat{f}_3^F, \tag{A4c}$$

$$\frac{\partial}{\partial t_1}\hat{f}_4^{eq} + \frac{\partial}{\partial x_1}\hat{f}_8^{eq} + \frac{\partial}{\partial y_1}\hat{f}_9^{eq} = -\hat{f}_4^F, \tag{A4d}$$

$$\frac{\partial}{\partial t_1}\hat{f}_5^{eq} + \frac{\partial}{\partial x_1}\hat{f}_{10}^{eq} + \frac{\partial}{\partial y_1}\hat{f}_{11}^{eq} = -s_5\hat{f}_5^{(1)} - \hat{f}_5^F, \tag{A4e}$$

$$\frac{\partial}{\partial t_1}\hat{f}_6^{eq} + \frac{\partial}{\partial x_1}\hat{f}_{11}^{eq} + \frac{\partial}{\partial y_1}\hat{f}_{12}^{eq} = -s_6\hat{f}_6^{(1)} - \hat{f}_6^F, \tag{A4f}$$

$$\frac{\partial}{\partial t_1}\hat{f}_7^{eq} + \frac{\partial}{\partial x_1}\hat{f}_{12}^{eq} + \frac{\partial}{\partial y_1}\hat{f}_{13}^{eq} = -s_7\hat{f}_7^{(1)} - \hat{f}_7^F, \tag{A4g}$$

$$\frac{\partial}{\partial t_1}\hat{f}_8^{eq} + \frac{\partial}{\partial x_1}\hat{f}_{14}^{eq} + \frac{\partial}{\partial y_1}\hat{f}_{15}^{eq} = -s_8\hat{f}_8^{(1)} - \hat{f}_8^F, \tag{A4h}$$

$$\frac{\partial}{\partial t_1}\hat{f}_9^{eq} + \frac{\partial}{\partial x_1}\hat{f}_{15}^{eq} + \frac{\partial}{\partial y_1}\hat{f}_{16}^{eq} = -s_9\hat{f}_9^{(1)} - \hat{f}_9^F. \tag{A4i}$$

From Eq. (A3c), we obtain

$$\frac{\partial}{\partial t_2}\hat{f}_1^{eq} = 0, \tag{A5a}$$

$$\frac{\partial}{\partial t_2}\hat{f}_2^{eq} + \frac{\partial}{\partial x_1}\hat{f}_5^{(1)} + \frac{\partial}{\partial y_1}\hat{f}_6^{(1)} = 0, \tag{A5b}$$

$$\frac{\partial}{\partial t_2}\hat{f}_3^{eq} + \frac{\partial}{\partial x_1}\hat{f}_6^{(1)} + \frac{\partial}{\partial y_1}\hat{f}_7^{(1)} = 0, \tag{A5c}$$

$$\frac{\partial}{\partial t_2}\hat{f}_4^{eq} + \frac{\partial}{\partial x_1}\hat{f}_8^{(1)} + \frac{\partial}{\partial y_1}\hat{f}_9^{(1)} = 0. \tag{A5d}$$

Adding Eqs.(A4a)–(A4d) and (A5a)–(A5d) leads to the following equations:

$$\frac{\partial}{\partial t}\hat{f}_1^{eq}+\frac{\partial}{\partial x}\hat{f}_2^{eq}+\frac{\partial}{\partial y}\hat{f}_3^{eq}=-\hat{f}_1^F, \tag{A6a}$$

$$\frac{\partial}{\partial t}\hat{f}_2^{eq}+\frac{\partial}{\partial x}\hat{f}_5^{eq}+\frac{\partial}{\partial y}\hat{f}_6^{eq}=-\hat{f}_2^F-\frac{\partial}{\partial x}\hat{f}_5^{(1)}-\frac{\partial}{\partial y}\hat{f}_6^{(1)}, \tag{A6b}$$

$$\frac{\partial}{\partial t}\hat{f}_3^{eq}+\frac{\partial}{\partial x}\hat{f}_6^{eq}+\frac{\partial}{\partial y}\hat{f}_7^{eq}=-\hat{f}_3^F-\frac{\partial}{\partial x}\hat{f}_6^{(1)}-\frac{\partial}{\partial y}\hat{f}_7^{(1)}, \tag{A6c}$$

$$\frac{\partial}{\partial t}\hat{f}_4^{eq}+\frac{\partial}{\partial x}\hat{f}_8^{eq}+\frac{\partial}{\partial y}\hat{f}_9^{eq}=-\hat{f}_4^F-\frac{\partial}{\partial x}\hat{f}_8^{(1)}-\frac{\partial}{\partial y}\hat{f}_9^{(1)}. \tag{A6d}$$

It is easily shown that the function f_i^F satisfies the similar moments

$$\iint f^F \mathrm{d}\boldsymbol{v}\mathrm{d}\eta=0=\sum f_i^F, \tag{A7a}$$

$$\iint f^F v_\alpha \mathrm{d}\boldsymbol{v}\mathrm{d}\eta=\rho g_\alpha=\sum f_i^F v_{i\alpha}, \tag{A7b}$$

$$\iint f^F \frac{(v^2+\eta^2)}{2}\mathrm{d}\boldsymbol{v}\mathrm{d}\eta=\rho g_\alpha u_\alpha=\sum f_i^F \frac{(v_i^2+\eta_i^2)}{2}, \tag{A7c}$$

$$\iint f^F v_\alpha v_\beta \mathrm{d}\boldsymbol{v}\mathrm{d}\eta=\rho g_\alpha u_\beta+\rho g_\beta u_\alpha=\sum f_i^F v_{i\alpha}v_{i\beta}, \tag{A7d}$$

$$\iint f^F \frac{(v^2+\eta^2)}{2}v_\alpha \mathrm{d}\boldsymbol{v}\mathrm{d}\eta=\rho\left[g_\beta u_\alpha u_\beta+\left(\frac{b+2}{2}RT+\frac{u^2}{2}\right)g_\alpha\right]=\sum f_i^F\frac{(v_i^2+\eta_i^2)}{2}v_{i\alpha}. \tag{A7e}$$

Equations (A7a)–(A7e) can be written in matrix form, i.e., $\hat{\boldsymbol{f}}^F=\boldsymbol{M}\boldsymbol{f}^F$, where $\hat{f}_1^F=0$, $\hat{f}_2^F=\rho g_x$, $\hat{f}_3^F=\rho g_y$, $\hat{f}_4^F=\rho(g_x u_x+g_y u_y)$, $\hat{f}_5^F=2\rho g_x u_x$, $\hat{f}_6^F=\rho(g_x u_y+g_y u_x)$, $\hat{f}_7^F=2\rho g_y u_y$, $\hat{f}_8^F=\rho[g_x u_x^2+g_y u_x u_y+g_x(\frac{b+2}{2}RT+\frac{u^2}{2})]$, $\hat{f}_9^F=\rho[g_y u_y^2+g_x u_x u_y+g_y(\frac{b+2}{2}RT+\frac{u^2}{2})]$, and the other terms $(i=10,\ldots,16)$ are 0.

Using the definitions of $\hat{f}_i^{eq}$ and $\hat{f}_i^F$, we can obtain

$$\frac{\partial\rho}{\partial t}+\frac{\partial(\rho u_\alpha)}{\partial x_\alpha}=0, \tag{A8a}$$

$$\frac{\partial(\rho u_\alpha)}{\partial t}+\frac{\partial(\rho u_\alpha u_\beta)}{\partial x_\beta}+\frac{\partial P}{\partial x_\alpha}=\frac{\partial}{\partial x_\beta}\left[\mu\left(\frac{\partial u_\alpha}{\partial x_\beta}+\frac{\partial u_\beta}{\partial x_\alpha}-\frac{2}{b}\frac{\partial u_\chi}{\partial x_\chi}\delta_{\alpha\beta}\right)\right]-\rho g_\alpha, \tag{A8b}$$

$$\frac{\partial e}{\partial t}+\frac{\partial}{\partial x_\alpha}[(e+P)u_\alpha]=\frac{\partial}{\partial x_\beta}\left[\left(\frac{b}{2}+1\right)\lambda' R\frac{\partial T}{\partial x_\beta}+\lambda'\left(\frac{\partial u_\alpha}{\partial x_\beta}+\frac{\partial u_\beta}{\partial x_\alpha}-\frac{2}{b}\frac{\partial u_\chi}{\partial x_\chi}\delta_{\alpha\beta}\right)u_\alpha\right]-\rho g_\alpha u_\alpha,\quad \alpha,\beta,\chi=x,y, \tag{A8c}$$

where $\mu=\rho RT/s_v$ ($s_v=s_5=s_6=s_7$) and $\lambda'=\rho RT/s_T$ ($s_T=s_8=s_9$).

By modifying the collision operators of the moments related to energy flux,

$$\hat{\boldsymbol{S}}_{88}(\hat{f}_8-\hat{f}_8^{eq})\Rightarrow\hat{\boldsymbol{S}}_{88}(\hat{f}_8-\hat{f}_8^{eq})+(s_T/s_v-1)\rho T u_x\times\left(2\frac{\partial u_x}{\partial x}-\frac{2}{b}\frac{\partial u_x}{\partial x}-\frac{2}{b}\frac{\partial u_y}{\partial y}\right)+(s_T/s_v-1)\rho T u_y\left(\frac{\partial u_y}{\partial x}+\frac{\partial u_x}{\partial y}\right), \tag{A9a}$$

$$\hat{\boldsymbol{S}}_{99}(\hat{f}_9-\hat{f}_9^{eq})\Rightarrow\hat{\boldsymbol{S}}_{99}(\hat{f}_9-\hat{f}_9^{eq})+(s_T/s_v-1)\rho T u_x\times\left(\frac{\partial u_y}{\partial x}+\frac{\partial u_x}{\partial y}\right)+(s_T/s_v-1)\rho T u_y\left(2\frac{\partial u_y}{\partial y}-\frac{2}{b}\frac{\partial u_x}{\partial x}-\frac{2}{b}\frac{\partial u_y}{\partial y}\right), \tag{A9b}$$

we get the following energy equation:

$$\frac{\partial e}{\partial t}+\frac{\partial}{\partial x_\alpha}[(e+P)u_\alpha]=\frac{\partial}{\partial x_\beta}\left[\lambda\frac{\partial T}{\partial x_\beta}+\mu\left(\frac{\partial u_\alpha}{\partial x_\beta}+\frac{\partial u_\beta}{\partial x_\alpha}-\frac{2}{b}\frac{\partial u_\chi}{\partial x_\chi}\delta_{\alpha\beta}\right)u_\alpha\right]-\rho g_\alpha u_\alpha, \tag{A10}$$

where $\lambda=(\frac{b}{2}+1)R\lambda'$.

References

1. L. Rayleigh, Investigation of the character of the equilibrium of an incompressible heavy fluid of variable density, *Proc. London Math. Soc.* s1–14(1), 170 (1882)
2. G. Taylor, The instability of liquid surfaces when accelerated in a direction perpendicular to their planes (I), *P. Roy. Soc. A* 201(1065), 192 (1950)
3. W. H. Ye, W. Y. Zhang, G. N. Chen, C. Q. Jin, and J. Zhang, Numerical simulations of the FCT method on Rayleigh–Taylor and Richtmyer–Meshkov instabilities, *Chin. J. Comput. Phys.* 15(3), 277 (1998)
4. X. L. Li, B. X. Jin, and J. Glimm, Numerical study for the three dimensional Rayleigh–Taylor instability through the TVD/AC scheme and parallel computation, *J. Comput. Phys.* 126(2), 343 (1996)
5. G. Tryggvason, B. Bunner, A. Esmaeeli, D. Juric, N. Al-Rawahi, W. Tauber, J. Han, S. Nas, and Y. J. Jan, A front-tracking method for the computations of multiphase flow, *J. Comput. Phys.* 169(2), 708 (2001)
6. Y. K. Li and A. Umemura, Mechanism of the large surface deformation caused by Rayleigh–Taylor instability at large Atwood number, *J. Appl. Math. Phys.* 2(10), 971 (2014)
7. M. S. Shadloo, A. Zainali, and M. Yildiz, Simulation of single mode Rayleigh–Taylor instability by SPH method, *Comput. Mech.* 51(5), 699 (2013)

8. L. Duchemin, C. Josserand, and P. Clavin, Asymptotic behavior of the Rayleigh–Taylor instability, *Phys. Rev. Lett.* 94(22), 224501 (2005)
9. A. W. Cook and P. E. Dimotakis, Transition stages of Rayleigh–Taylor instability between miscible fluids, *J. Fluid Mech.* 443, 69 (2001)
10. A. Celani, A. Mazzino, and L. Vozella, Rayleigh–Taylor turbulence in two dimensions, *Phys. Rev. Lett.* 96(13), 134504 (2006)
11. W. Cabot, Comparison of two- and three-dimensional simulations of miscible Rayleigh–Taylor instability, *Phys. Fluids* 18(4), 045101 (2006)
12. A. Celani, A. Mazzino, P. Muratore-Ginanneschi, and L. Vozella, Phase-field model for the Rayleigh–Taylor instability of immiscible fluids, *J. Fluid Mech.* 622, 115 (2009)
13. R. Betti and J. Sanz, Bubble acceleration in the ablative Rayleigh–Taylor instability, *Phys. Rev. Lett.* 97(20), 205002 (2006)
14. M. R. Gupta, L. Mandal, S. Roy, and M. Khan, Effect of magnetic field on temporal development of Rayleigh–Taylor instability induced interfacial nonlinear structure, *Phys. Plasmas* 17(1), 012306 (2010)
15. P. K. Sharma, R. P. Prajapati, and R. K. Chhajlani, Effect of surface tension and rotation on Rayleigh–Taylor instability of two superposed fluids with suspended particles, *Acta Phys. Pol. A* 118(4), 576 (2010)
16. R. Banerjee, L. K. Mandal, S. Roy, M. Khan, and M. R. Gupta, Combined effect of viscosity and vorticity on single mode Rayleigh–Taylor instability bubble growth, *Phys. Plasmas* 18(2), 022109 (2011)
17. H. Liu, W. Kang, Q. Zhang, Y. Zhang, H. Duan, and X. T. He, Molecular dynamics simulations of microscopic structure of ultra strong shock waves in dense helium, *Front. Phys.* 11(6), 115206 (2016)
18. S. Succi, The Lattice Boltzmann Equation for Fluid Dynamics and Beyond, Oxford: Oxford University Press, 2001
19. R. Benzi, S. Succi, and M. Vergassola, The lattice Boltzmann equation: Theory and applications, *Phys. Rep.* 222(3), 145 (1992)
20. A. Xu, G. Gonnella, and A. Lamura, Phase-separating binary fluids under oscillatory shear, *Phys. Rev. E* 67(5), 056105 (2003)
21. A. G. Xu, G. Gonnella, and A. Lamura, Morphologies and flow patterns in quenching of lamellar systems with shear, *Phys. Rev. E* 74(1), 011505 (2006)
22. A. G. Xu, G. Gonnella, and A. Lamura, Simulations of complex fluids by mixed lattice Boltzmann-finite difference methods, *Physica A* 362(1), 42 (2006)
23. X. Shan and H. Chen, Lattice Boltzmann model for simulating flows with multiple phases and components, *Phys. Rev. E* 47(3), 1815 (1993)
24. X. Shan and H. Chen, Simulation of nonideal gases and liquid-gas phase transitions by the lattice Boltzmann equation, *Phys. Rev. E* 49(4), 2941 (1994)
25. G. Gonnella, E. Orlandini, and J. M. Yeomans, Spinodal decomposition to a lamellar phase: Effects of hydrodynamic flow, *Phys. Rev. Lett.* 78(9), 1695 (1997)
26. H. Fang, Z. Wang, Z. Lin, and M. Liu, Lattice Boltzmann method for simulating the viscous flow in large distensible blood vessels, *Phys. Rev. E* 65(5), 051925 (2002)
27. Z. Guo and C. Shu, Lattice Boltzmann Method and Its Applications in Engineering (advances in computational fluid dynamics), World Scientific Publishing Company, 2013
28. A. Xu, G. Zhang, Y. Li, and H. Li, Modeling and simulation of nonequilibrium and multiphase complex systems-lattice Boltzmann kinetic theory and application, *Prog. Phys.* 34(3), 136 (2014)
29. R. Zhang, Y. Xu, B. Wen, N. Sheng, and H. Fang, Enhanced permeation of a hydrophobic fluid through particles with hydrophobic and hydrophilic patterned surfaces, *Sci. Rep.* 4, 5738 (2014)
30. X. B. Nie, Y. H. Qian, G. D. Doolen, and S. Y. Chen, Lattice Boltzmann simulation of the two-dimensional Rayleigh–Taylor instability, *Phys. Rev. E* 58(5), 6861 (1998)
31. X. Y. He, S. Y. Chen, and R. Y. Zhang, A lattice Boltzmann scheme for incompressible multiphase flow and its application in simulation of Rayleigh–Taylor instability, *J. Comput. Phys.* 152(2), 642 (1999)
32. X. Y. He, R. Y. Zhang, S. Y. Chen, and G. D. Doolen, On the three-dimensional Rayleigh–Taylor instability, *Phys. Fluids* 11(5), 1143 (1999)
33. R. Y. Zhang, X. Y. He, and S. Y. Chen, Interface and surface tension in incompressible lattice Boltzmann multiphase model, *Comput. Phys. Commun.* 129(1-3), 121 (2000)
34. Q. Li, K. H. Luo, Y. J. Gao, and Y. L. He, Additional interfacial force in lattice Boltzmann models for incompressible multiphase flows, *Phys. Rev. E* 85(2), 026704 (2012)
35. G. J. Liu and Z. L. Guo, Effects of Prandtl number on mixing process in miscible Rayleigh–Taylor instability: A lattice Boltzmann study, *Int. J. Numer. Method. H.* 23(1), 176 (2013)
36. H. Liang, B. C. Shi, Z. L. Guo, and Z. H. Chai, Phase-field-based multiple-relaxation-time lattice Boltzmann model for incompressible multiphase flows, *Phys. Rev. E* 89(5), 053320 (2014)
37. M. Sbragaglia, R. Benzi, L. Biferale, H. Chen, X. Shan, and S. Succi, Lattice Boltzmann method with self-consistent thermo-hydrodynamic equilibria, *J. Fluid Mech.* 628, 299 (2009)

38. A. Scagliarini, L. Biferale, M. Sbragaglia, K. Sugiyama, and F. Toschi, Lattice Boltzmann methods for thermal flows: Continuum limit and applications to compressible Rayleigh–Taylor systems, *Phys. Fluids* 22(5), 055101 (2010)
39. L. Biferale, F. Mantovani, M. Sbragaglia, A. Scagliarini, F. Toschi, and R. Tripiccione, Reactive Rayleigh–Taylor systems: Front propagation and non-stationarity, *Europhys. Lett.* 94(5), 54004 (2011)
40. A. Xu, G. Zhang, Y. Gan, F. Chen, and X. Yu, Lattice Boltzmann modeling and simulation of compressible flows, *Front. Phys.* 7(5), 582 (2012)
41. B. Yan, A. Xu, G. Zhang, Y. Ying, and H. Li, Lattice Boltzmann model for combustion and detonation, *Front. Phys.* 8(1), 94 (2013)
42. C. Lin, A. Xu, G. Zhang, and Y. Li, Polar coordinate lattice Boltzmann kinetic modeling of detonation phenomena, *Commum. Theor. Phys.* 62(5), 737 (2014)
43. A. Xu, C. Lin, G. Zhang, and Y. Li, Multiple-relaxation-time lattice Boltzmann kinetic model for combustion, *Phys. Rev. E* 91(4), 043306 (2015)
44. A. Xu, G. Zhang, and Y. Ying, Progess of discrete Boltzmann modeling and simulation of combustion system, *Acta Phys. Sin.* 64(18), 184701 (2015)
45. C. Lin, A. Xu, G. Zhang, and Y. Li, Double-distribution-function discrete Boltzmann model for combustion, *Combust. Flame* 164, 137 (2016)
46. Y. Zhang, A. Xu, G. Zhang, C. Zhu, and C. Lin, Kinetic modeling of detonation and effects of negative temperature coefficient, *Combust. Flame* (2016) (in press)
47. Y. Gan, A. Xu, G. Zhang, and S. Succi, Discrete Boltzmann modeling of multiphase flows: Hydrodynamic and thermodynamic non-equilibrium effects, *Soft Matter* 11 11(26), 5336 (2015)
48. C. Lin, A. Xu, G. Zhang, Y. Li, and S. Succi, Polar-coordinate lattice Boltzmann modeling of compressible flows, *Phys. Rev. E* 89(1), 013307 (2014)
49. F. Chen, A. Xu, G. Zhang, Y. Wang, Two-dimensional MRT LB model for compressible and incompressible flows, *Front. Phys.* 9(2), 246 (2014)
50. H. Lai, A. Xu, G. Zhang, Y. Gan, Y. Ying, and S. Succi, Thermo-hydrodynamic non-equilibrium effects on compressible Rayleigh–Taylor instability, arXiv: 1507.01107
51. D. Layzer, On the instability of superposed fluids in a gravitational field, *Astrophys. J.* 122, 1 (1955)
52. S. F. Li, W. H. Ye, Y. Zhang, S. Shu, and A. G. Xiao, High order FD-WENO schemes for Rayleigh–Taylor instability problems, *Chin. J. Comput. Phys.* 25(4), 379 (2008)
53. D. Youngs, Numerical simulation of turbulent mixing by Rayleigh–Taylor instability, *Physica D* 12(1–3), 32 (1984)
54. Y. D. Zhang, Modeling and research of detonation based on discrete Boltzmann method, A Dissertation Submitted for the Degree of Master, Beihang University, 2015